Comparative Study on the Effect of Leading Edge Protuberance of Different Shapes on the Aerodynamic Performance of Two Distinct Airfoils

C. Jayapal Reddy and A. Sathyabhama[†]

Department of Mechanical Engineering, NITK Surathkal, Mangalore – 575025, Karnataka, India

†*Corresponding Author Email: sathyabhama@nitk.edu.in*

ABSTRACT

This study investigated the effect of leading-edge protuberances on the aerodynamic performance of two distinct airfoils with low Reynold's number (Re): E216 and SG6043. Three protuberance shapes, namely sinusoidal, slot, and triangular, were considered. The amplitudes (A) of protuberances considered were $0.03c$, $0.06c$, and $0.11c$, and the wavelengths (W) were $0.11c$, $0.21c$, and $0.43c$, where c is the chord of the airfoil. The numerical and experimental analyses were performed in the angle of attack (AoA) range of 0° to +20° at and Re of 10^5. The numerical investigation was performed using the commercial computational fluid dynamics package ANSYS FLUENT. The SST k-ω model was used to simulate turbulent flow. The experimental force measurements were conducted using a highly sensitive three-component force balance in a subsonic wind tunnel facility. The flow physics was analyzed using vorticity contours in streamwise and spanwise slices and static pressure distribution contours. The smoke flow visualization technique was used to observe flow streamlines, boundary layer separation, and reattachment over the airfoil surface. The result indicated that the triangular and slot protuberances were the most beneficial for improving poststall lift and reducing skin friction drag. The operating mechanism involved a shift in pressure distribution due to leading-edge alterations and flow energization by secondary flow emanating from the protuberances.

Keywords: Tubercles; Passive flow control; Separation control; Airfoil performance; Post-stall improvement; Stall delay; Biomimicry.

NOMENCLATURE

A	amplitude	q_∞	freestream dynamic pressure
a	airfoil planform area	Re	Reynolds number = $\rho\, c\, v_\infty/\mu$
c	chord	s	airfoil span
C_d	drag coefficient = $D/q_\infty\, a$	$(t/c)_{max}$	maximum thickness to chord ratio
C_l	lift coefficient = $L/q_\infty\, a$	v_∞	freestream mean velocity
$C_{l\,max}$	maximum lift coefficient	W	wavelength
C_P	pressure coefficient	x	distance along chord from the leading edge
D	drag force		
k	turbulent kinetic energy	ρ	air density
L	lift force	α	angle of attack
L/D	lift to drag ratio	μ	dynamic viscosity
$(L/D)_{max}$	maximum lift to drag ratio	ω	turbulent dissipation rate

1. INTRODUCTION

In recent years, the leading-edge protuberance modifications on airfoils or wings have attracted attention as a new passive control technique. This concept was inspired by the morphological features of humpback whales. The agility of whales is partially attributed to their pectoral flippers with leading-edge protuberances. Moreover, the profile of the mean cross-section of flippers is similar to that of an NACA 634-021 airfoil, and the leading-edge profile along the spanwise direction can be approximated as a sinusoidal-wave shape (Fig. 1). Miklosovic *et al.* (2004) experimentally investigated

the hydrodynamic performance of a humpback whale flipper model at a Reynold's number (Re) of 5×10^5. The authors determined an increase in the maximum lift and stall angle. Since then, many studies have investigated the effects of leading-edge protuberances on full-span airfoil performance. Empirical and computational studies (Fish 2020) have indicated that tubercles passively modify the flow over wing-like structures. The flow between the tubercles generates counter-rotating vortices in a sacrificed separation, which assists in energizing the flow over the tubercles. The tubercle-induced flow pattern over a wing increases the lift, delays the stall, and maintains a low drag after the stall.

Fig. 1. Left: Humpback Whale and right: Whale Pectoral flipper (Corsini *et al*. 2013).

Experimental and numerical studies investigating the effect of tubercles over a range of Re have indicated that the effect of tubercles depends on the type of the model (i.e., two-dimensional airfoils or three-dimensional wings). The aerodynamic performance of airfoils incorporated with tubercles was more favorable only in the post stall region (Johari *et al.* 2007, Miklosovic *et al.* 2007, Hansen *et al.* 2011, Zhang *et al.* 2013, 2014, Cai *et al.* 2015, Custodio *et al.* 2015, New *et al.* 2015, Sreejith and Sathyabhama 2020). The improved aerodynamic performance can be attributed to streamwise vortices.

Studies using humpback whale flipper models have observed increases in the maximum lift coefficient and post stall lift, a delay in the stall, and a decrease in the drag (Miklosovic *et al.* 2004, 2007, Stanway 2008, Carreira Pedro and Kobayashi 2008). Previous studies on three-dimensional wings have reported different findings for different configurations, including a rectangular or tapered planform, swept or unswept wings, and full-span or semi-span models (Bolzon *et al.* 2017, Wei *et al.* 2018, Weber *et al.* 2010, Guerreiro and Sousa 2012, Joseph *et al.* 2022). However, the mechanism of tubercles involved flow energization by counter-rotating vortices.

Previous research on the aerodynamic performance of different airfoils and tubercle geometrical arrangements have found improvement in lift and drag coefficients in the post stall region. This positive effect is useful in wind turbine applications because operating wind turbines at higher wind speeds without a stall can increase power generation. Many studies have focused only on sinusoidal and wavy protuberances. No study has explored the flow process involving airfoil selection, tubercle shape,

and geometrical modifications in low Re flows. Thus, this study investigated the aerodynamic performance of several leading-edge protuberance shapes, namely sinusoidal, triangular, and slots, on two low-Re airfoils, E216 and SG6043. The amplitude (A) and wavelength (W) of protuberances were selected based on the morphological properties of the flipper of humpback whales. A numerical study was performed using the commercial CFD package ANSYS FLUENT in the angle-of-arrival (AoA) range of 0° to +20°. Turbulence was modeled using the shear stress transport (SST) k-ω model. Experimental force measurements were performed in a subsonic wind tunnel facility with a highly sensitive three-component force balance.

2. METHODOLOGY

2.1 Airfoil Selection

The aerodynamic behavior of 12 airfoils (Siram *et al.* 2022) was examined using XFOIL and QBlade tools, and E216 was determined to have the highest lift to drag (L/D) ratio at a low Re, followed by SG6043. Furthermore, considering the maximum L/D ratio, maximum lift coefficient ($C_{l\ max}$), and stall angle (α_{stall}) obtained from XFOIL (Drela and Youngren 2001), E216 had an L/D)$_{max}$ of 68.5, a $C_{l\ max}$ of 1.5706, and an α_{stall} of 13.5° at an Re of 10^5, whereas SG6043 profile had an L/D)$_{max}$ of 66.5, a $C_{l\ max}$ of 1.6491, and a α_{stall} of 14.5°. Thus, these two airfoils were selected for the present study.

Table 1 Geometrical parameters of the airfoil profiles

Parameters	SG6043	E216 (10.4%)
Thickness (%)	9.990	10.408
Camber (%)	5.498	5.169
Trailing Edge Angle (%)	10.646	8.688
Lower Surface Flatness (%)	18.685	14.584
Leading Edge Radius (%)	2.347	2.215

Table 1 illustrates the geometrical parameters of the two airfoils, and Fig. 2 presents their profiles. E216 and SG6043 airfoils (Siram *et al.* 2022; Chaudhary and Prakash 2021; Gupta *et al.* 2017; Jin and Lee 2015) used in small horizontal axis wind turbines operating at a low Re exhibited better aerodynamic performance, maximum L/D ratio, and maximum C_l.

2.2 Computational Details

2.2.1 Leading-edge protuberance modelling

The SOLIDWORKS design tool was used to create baseline and various leading-edge protuberance models for the E216 and SG6043 profiles. The baseline model of both the profiles was developed by extruding the curve obtained by joining the airfoil coordinates to a span(x) of 0.132 m. The sinusoidal protuberance model was developed by lofting the equation-driven curve with the same span as the

SG6043

E216 (10.4%)
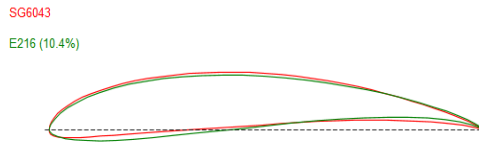
Fig. 2. SG6043 and E216 airfoil profiles.

baseline model by using Eq. (1), where A and W are the amplitude and wavelength of the protuberances, respectively. The triangular and slot protuberance models were created similarly, but the leading-edge profile was drawn to achieve the desired shape. In this study, the amplitude values selected were $0.03c$, $0.06c$, and $0.11c$ and the wavelengths were $0.11c$, $0.21c$, and $0.43c$, where c is the chord of the airfoil. These values are defined concerning a reference chord(c) of 0.15 m. For the slot protuberance, the thickness (t) was maintained constant at 0.002 m. Figure 3 presents the baseline and protuberance models of the E216 airfoil (top view). Table 2 lists the various protuberance configurations and terminology used in this study.

$$y_x = A \sin bx, \text{ where } b = \frac{2\pi}{W} \qquad (1)$$

Table 2 Protuberance configurations and their terminology

Configuration	Terminology	A/W ratio
A = $0.03c$, W = $0.11c$	A4.5W16.5	0.27
A = $0.03c$, W = $0.21c$	A4.5W31.5	0.14
A = $0.03c$, W = $0.43c$	A4.5W64.5	0.07
A = $0.06c$, W = $0.11c$	A9W16.5	0.54
A = $0.06c$, W = $0.21c$	A9W31.5	0.28
A = $0.06c$, W = $0.43c$	A9W64.5	0.14
A = $0.11c$, W = $0.11c$	A16.5W16.5	1
A = $0.11c$, W = $0.21c$	A16.5W31.5	0.52
A = $0.11c$, W = $0.43c$	A16.5W64.5	0.25

2.2.2 Boundary conditions and numerical setup

Figure 4 presents boundary conditions and computational domains with an unstructured mesh. In numerical studies, Ansys Fluent was used to create the fluid domain and meshing. To achieve a fully developed flow, the total length of the computational domain was set to 10 times the chord length, with a semicircular inlet with a radius of five times that of the chord length and a width of 10 times that of the chord length. A semicircular inlet domain was created to reduce computational time, and a fine mesh was generated around the airfoil by using the sphere of influence technique. Mesh resolution was higher near the airfoil, where a higher computational accuracy is required (Fig. 4). The height of the first cell adjacent to the surface was set to result in a y⁺ value less than one, as required by the turbulent models used. The height of the first cell was calculated using the y⁺ calculator (Eleni *et al.* 2012).

Unstructured mesh based on tetrahedral elements was chosen because the complex leading-edge geometry consists of distinct protuberances, including sinusoidal, triangular, and slots, with varying amplitudes and wavelengths. The boundary conditions were as follows: The inlet condition was considered as a velocity inlet on the domain's semicircular surface, the outlet condition was considered as a pressure outlet on the domain's outer vertical surface, with the outlet pressure being atmospheric pressure, and the no-slip condition was considered on the airfoil surface and outer horizontal surfaces. The semi-implicit method for pressure-linked equations algorithm proposed by Patankar (2018) was used to determined velocity and pressure fields, and the SST k-ω model was employed for turbulence modeling. For spatial discretization, least squares cell-based gradient and second-order upwind methods (FLUENT 2014) were used. All simulations were performed at an Re of 10^5, with AoA ranging from 0° to +20°. The free stream inlet velocity of air was calculated to be 10.8 m/s, and the flow was incompressible. The least square cell method was used for the spatial gradient, and the residual value of 10^{-5} was set as convergence criteria.

2.2.3 Turbulence modelling and governing equations

Extensive numerical studies on the tubercle effect have been conducted using computational models such as RANS, DES, LES, and hybrid RANS-LES (Rostamzadeh *et al.* 2013; Skillen *et al.* 2013; Fernandes *et al.* 2013). Although models such as LES and DES can accurately predict counter-rotating vortices generated by these tubercles (Skillen *et al.* 2013; Fernandes *et al.* 2013), they have a high computational cost and are rarely used in simulations. Thus, cheaper yet more accurate RANS-based models should be developed for performing flow analysis on tubercle airfoils. RANS models have proven to be effective, efficient, and accurate in predicting the flow field, despite not being as accurate as LES and DES models.

Versteeg and Malalasekera (2007) presented governing equations for the model constants of the corresponding model. Gawad (2013) reported that time-averaged continuity and momentum equations control the flow around an airfoil model. The k-ω based SST model allows for turbulent shear stress transmission and provides extremely accurate estimates of the onset and severity of flow separation under unfavorable pressure gradients. The simple k-ω model incorporates the benefits of the Wilcox and k-ϵ models but still fails to anticipate the beginning and magnitude of flow separation from smooth surfaces. One such gap arises primarily because these models fail to account for turbulent shear stress transfer, which overpredicts eddy viscosity. Thus, the required transport behavior can be determined by including a limiter in the eddy-viscosity formulation, as shown in Eq. (2).

$$\nu_t = \frac{a_1 k}{\max(a_1 \omega SF)} \qquad (2)$$

where F is a blending function used to mix the k-ω model at the surface with the k-ϵ model in the outside

(a) Baseline model

(b) Triangular model

(c) Sinusoidal model

(d) Slots model
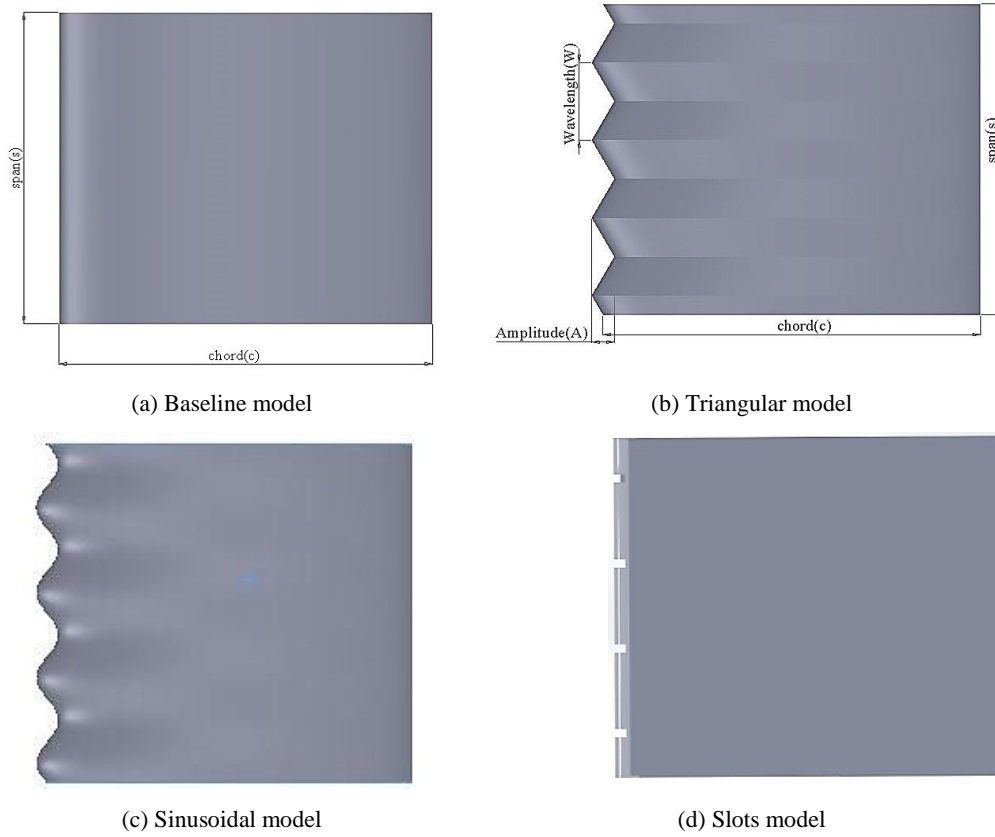
Fig. 3. E216 airfoil top view of three-dimensional models.
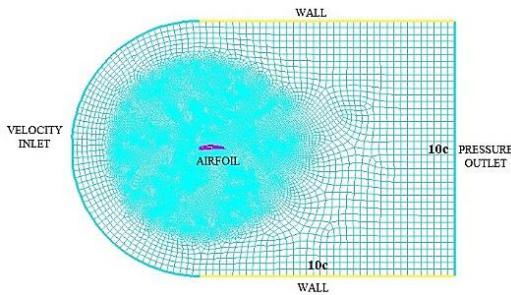
Fig. 4. Computational domain and boundary conditions with a far field length of 10c.

area established by Menter *et al*. (2003). This requires converting the $k\text{-}\epsilon$ model to a $k\text{-}\omega$ formulation and incorporating the required equations. S is an independent strain rate measure.

The SST $k\text{-}\omega$ model is identical to the regular $k\text{-}\omega$ model in terms of its structure. However, the transition model interacts with the SST turbulence model by making the following changes to the k-equation:

$$\frac{\partial}{\partial t}(\rho k) + \frac{\partial}{\partial x_i}(\rho k u_i) = \frac{\partial}{\partial x_j}\left(\Gamma_k \frac{\partial k}{\partial x_j}\right) + \tilde{G}_k - Y_k + S_k \tag{3}$$

The transport equation for the intermittency term ω is given in Eq. (4).

$$\frac{\partial}{\partial t}(\rho \omega) + \frac{\partial}{\partial x_i}(\rho \omega u_i) = \frac{\partial}{\partial x_j}\left(\Gamma_\omega \frac{\partial \omega}{\partial x_j}\right) + G_\omega - Y_\omega + D_\omega + S_\omega \tag{4}$$

Equations (3) and (4) $\tilde{G}_k$ represent the generation of turbulence kinetic energy (k) due to mean velocity gradients. G_ω represent the generation of a specific rate of dissipation (ω). Γ_k and Γ_ω represents the effective diffusivity of k and ω, respectively. Y_k and Y_ω represents the dissipation of k and ω due to turbulence. D_ω represent the cross-diffusion term. S_k and S_ω are user-defined source terms.

2.2.4 Grid generation and mesh sensitivity analysis

A three-dimensional unstructured grid was developed using tetrahedral elements. For accurate capture and mapping of the airfoil wake profile, a zone of local grid refinement around the airfoil was generated using a sphere of influence with a radius of $4c$. At the walls, y+ was maintained at a value of less than one to accurately capture near-wall effects. The grid study for the baseline model of the E216 profile at an AoA of 0° is presented in Fig. 5.

The selected grid sizes for baseline range from 1 lakh to 16 lakh. For the convergence study, the variation in the coefficient of lift and drag values with the grid number of elements was investigated. Figure 5 presents a linear variation in C_l and C_d from G1 to G4, after which curves were nearly straight. The average variation in C_l and C_d from G3 to G4 was

5.45%, and the variation between grids G4 and G5 was 1.35%. Thus, grid G4 was chosen for the numerical analysis to examine the flow characteristics and aerodynamic performance of airfoils. Table 3 summarizes information on the grids that were used.
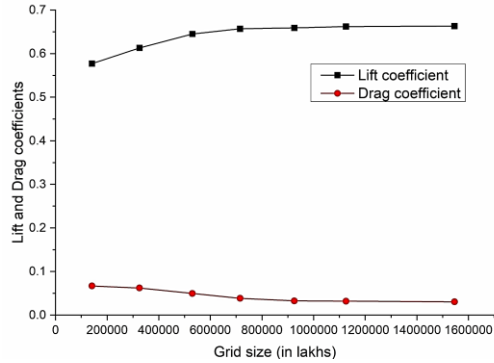
Fig. 5. Grid independence study for E216 profile at 0° AoA.

2.3 Experimental Setup and Techniques

2.3.1 Airfoil models

The airfoil models used for experimentation were fabricated using a 5-axis CNC milling machine with medium-density fibreboard wood as the material. The models selected for experimentation had baseline and $A9W64.5$ configuration with sinusoidal, triangular, and slots as leading-edge modifications (Fig. 6a).

Table 3 Details of grid convergence

Grid	No. of elements	Max. y^+	Aerodynamic coefficients	
			C_l	C_d
G1	1,41,054	0.2	0.597	0.0668
G2	3,25,460	0.2	0.613	0.0621
G3	5,30,240	0.2	0.645	0.0426
G4	7,15,025	0.2	0.657	0.0384
G5	9,25,457	0.2	0.659	0.0375
G6	11,25,458	0.2	0.662	0.0362
G7	15,45,789	0.2	0.663	0.0359

(a)   **(b)**
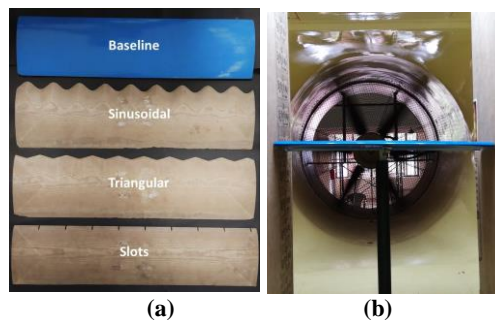
Fig. 6. (a) Experimental airfoil models (b) Airfoil mounting arrangement in the test section.

The amplitude to wavelength (A/W) ratio was 0.14. All the airfoil models were semi-span models with a span of 0.592 m and a mean chord of 0.15 m, resulting in a platform area of 0.08 m². Because the airfoil models are semi-span models, two wooden sheets are attached at the ends of the model (Fig. 6 b), with a gap of 0.002 m. These sheets prevent the formation of tip vortices so that semi-span models act similar to 2D airfoil sections. The blockage ratio due to wooden partition, airfoil model, and mounting arrangement is less than 10%. Hence, blockage corrections are not made for experimental results (Schreck *et al.* 2007; Chen and Liou 2011).

2.3.2 Subsonic wind tunnel facility

The experiments were performed in an open circuit, subsonic suction-type wind tunnel shown in Fig. 7 (a). The tunnel has a cross-section of 1 m × 1 m and a length of 2 m, with a maximum airflow speed of 30 m/s. The tunnel is a suction type, with a less than 0.12% turbulence level in the empty test section across the tunnel's operating range. The required velocity can be obtained by setting the corresponding RPM of the axial flow fan by using the wind tunnel calibration chart (Fig. 7b). The test section velocity was measured using a Pitot static tube placed at the entry of the test section. On the basis of the test section velocity of 10.8 m/s and a mean chord length of 0.15 m, the Re of 10^5 was set. The wind tunnel specifications are listed in Table 4.

(a)
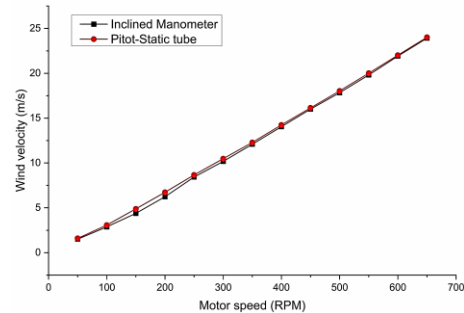
(b)

Fig. 7. (a) Subsonic wind tunnel facility (b) Wind tunnel calibration chart.

2.3.3 Aerodynamic force measurement

A highly sensitive three-component force balance was employed to measure the aerodynamic force

Table 4 Subsonic wind tunnel specifications

Parameter	Value
Test section dimensions	1m*1m*2m
Contraction ratio	9:1
Axial fan motor rpm(maximum)	720
Flow velocity(maximum)	30 m/s
Turbulence intensity(approximately)	0.12% (at 10m/s)
Axial fan capacity	Three phase, 15A, 440V, AC supply

generated by the airfoil model (Fig. 8). The design loads of the balance were 15 kg of normal force and 3 kg of drag force with an accuracy of 0.5%. The data were averaged over 1 min and collected using a 16 - bit data acquisition system.

The airfoil model was mounted on the stem that protrudes into the test section and has a simple mechanism for pitching the model. The stem was fixed on a metric plate that transfers the load onto four strain elements. Appropriately designed amplifiers can amplify outputs from the strain gauge mounted on strain elements. The measured voltages are converted into corresponding forces and moments by using Eq. (5), where D_{ij} represents the inverted matrix of C_{ij}, which is the calibration coefficient matrix. The gain in the denominator is attributable to the conversion of voltages to those at strain elements. The obtained aerodynamic forces are converted into nondimensional coefficients by using Eq. (6). The experimental uncertainties of the derived quantities were calculated using the technique reported by Kline (1953), and the lift and drag coefficients were determined to be ±3.56% and ±4.14%, respectively.

$$
\left.
\begin{aligned}
L &= (D_{11}V_1 + D_{12}V_2 + D_{13}V_3)1000/G \\[4pt]
P_m &= (D_{21}V_1 + D_{22}V_2 + D_{23}V_3)1000/G \\[4pt]
D &= (D_{31}V_1 + D_{32}V_2 + D_{33}V_3)1000/G
\end{aligned}
\right\} \quad (5)
$$

$$
C_l = \frac{L}{\frac{1}{2}\rho V_\infty^2 a} \;\; ; \quad C_d = \frac{D}{\frac{1}{2}\rho V_\infty^2 a} \tag{6}
$$

The force balance was calibrated to determine the relationship between measured forces (lift and drag) and the pitching moment against applied loads. The relationship was linear because of strain gauge instrumentation. The slopes of these linear variations were used to calculate calibration coefficients. The calibration body mounted on the balance and the associated microcontroller measurement system are presented in Fig. 9. The calibration curves were plotted by measuring voltages corresponding to the pure lift, drag, and moment loads. Fig. 10a and 10b present the lift and drag calibration curves, respectively. The value of D_{ij} obtained is given in Eq. (7).

$$
D_{ij} = \left.
\begin{bmatrix}
-1.9595 & -2.0625 & 0.2352 \\
-17.2651 & 11.5158 & -50.6412 \\
0.1080 & 0.0163 & 0.8266
\end{bmatrix}
\right\} \quad (7)
$$

2.3.4 Boundary layer analysis

The boundary layer probe consisted of 20 stainless steel tubes with a 0.25-mm internal diameter, inclined down at 15° (Fig.11 (a) and (b)) to capture pressure distribution close to the wind tunnel wall. The pressure was measured at 20 vertical positions simultaneously by using an electronic pressure transducer. Table 5 summarizes information on probes' locations. This experiment was performed to determine the standard flow quality of the tunnel to provide reliable data and measurements. The test section velocity was measured using a Pitot static tube. The local velocity (u) was measured at various positions in the vertical direction (y) from the wind tunnel wall surface until it equaled 0.99 times the free stream velocity (U_∞). The boundary layer profile (u/U_∞) plotted against the similarity variable (ξ) is presented in Fig. 11 (c). Nondimensional distance (ξ) is defined in Eq. (8).

$$
\xi = \frac{y}{2x}\sqrt{Re_x} \tag{8}
$$
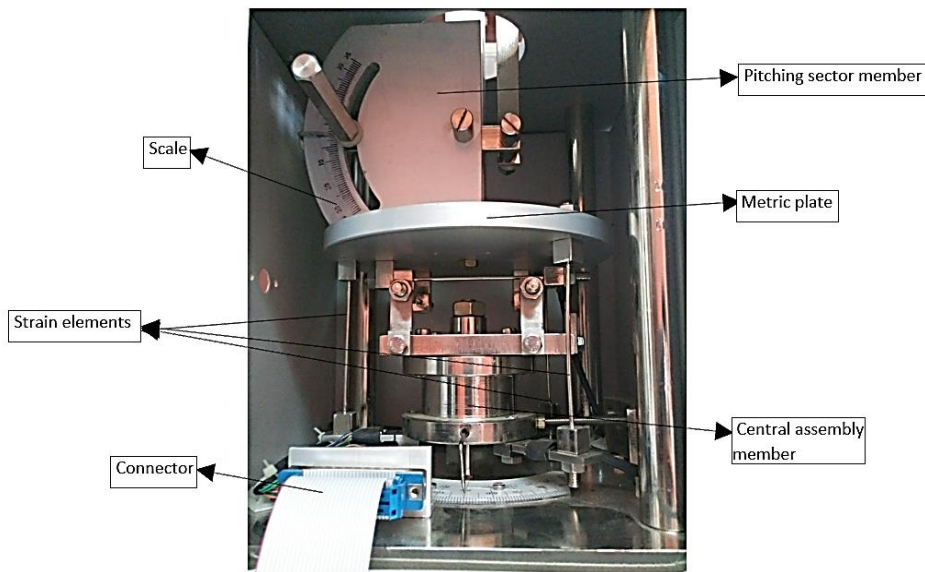
Fig. 8. Three component force balance system.
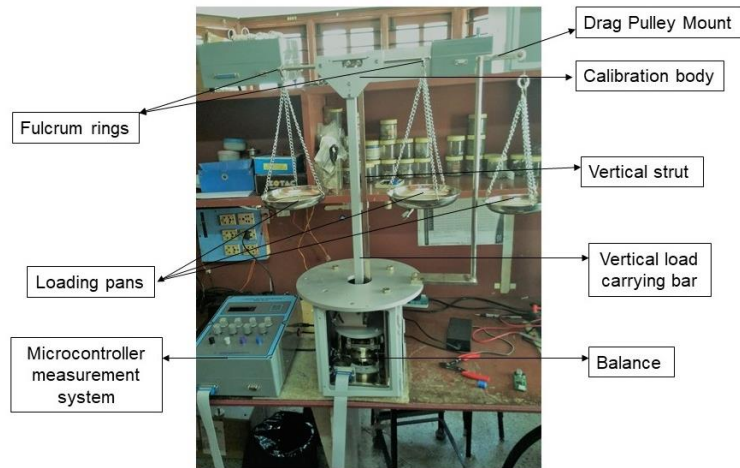
Fig. 9. Force balance calibration setup.

(a) Lift curve

(b) Drag curve
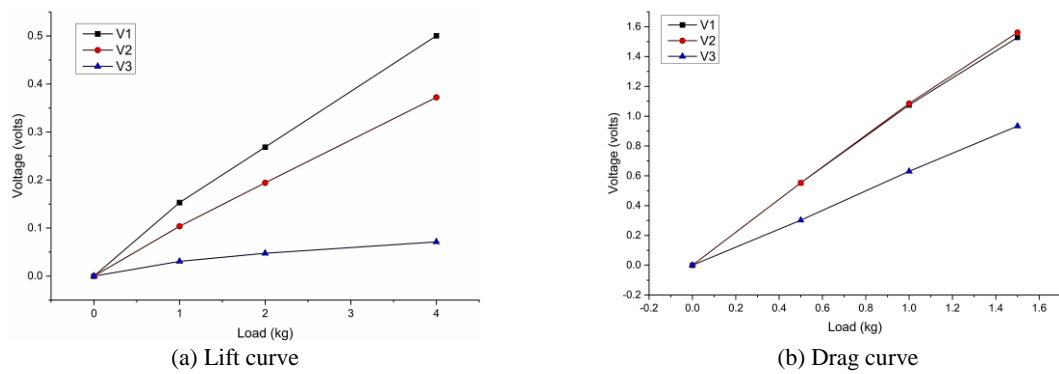
Fig. 10. Calibration curves.

Table 5 Probe locations for boundary layer measurement.

Probe number	1	2	3	4	5	6	7	8	9	10	11	12	13	14	15	16	17	18	19	20
Distance (mm)	0.5	1	2	3.5	4	5.5	7.5	9	11	13	14.5	16	18	20	22	24	27	28	31	34.5

We used Eq. (9) and (10) to calculate the boundary layer thickness (δ^*) and momentum thickness (θ) for this vertical distance.

$$\delta^* = \int_0^\delta \left(1 - \frac{u}{U_\infty}\right) dy \qquad (9)$$

$$\theta = \int_0^\delta \frac{u}{U_\infty}\left(1 - \frac{u}{U_\infty}\right) dy \qquad (10)$$

These equations were solved analytically by using the trapezoidal rule. According to the calculations, the boundary layer thickness was 35.01 mm, and the momentum thickness was 26.73 mm from the wall. Thus, the ratio of these two thicknesses was 1.31, which is ≤1.4; hence, the boundary layer was turbulent.

2.3.5 Smoke Generator

A smoke generator was used to visualize flow patterns by producing a thick white smoke in the direction of air movement over the airfoil models. The smoke generator equipment (Fig. 12) comprises a liquid reservoir, heating zone, smoke tube with control valves, and a blower/compressor beneath the control unit to propel smoke into the test area. Table

6 presents the detailed specifications and capacity of the smoke generator.

Table 6 Smoke generator specifications

Parameter	Value
Heater capacity	1 kW
Glass beaker oil capacity	500 ml
Oil drain capacity	200 ml
Smoke collecting jar	2000 ml
Blower capacity	0.24 HP, single phase, 2800 RPM

3. RESULTS AND DISCUSSION

3.1 Numerical validation

Simulation results were validated against experimental results for the E16 baseline airfoil model. The C_l, C_d, and L/D values obtained from the experiments and simulations were plotted against the

163

(a)   (b)

(c)
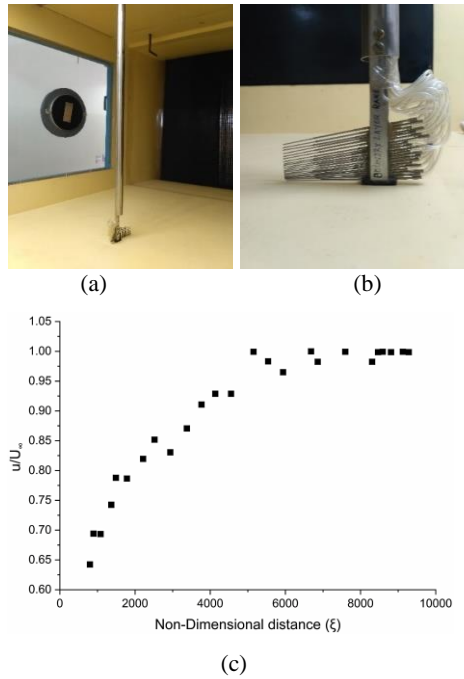
Fig. 11. (a)Total pressure tube rake inside the test section of wind tunnel (b) close view of the rake (c) Boundary layer profile.

(a) Front view.   (b) Rear view.
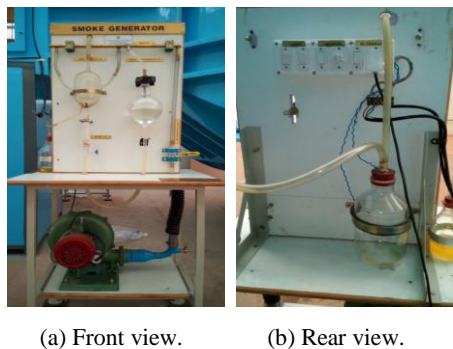
Fig. 12. Smoke generator.

AoA (Fig. 13). An acceptable agreement was noted between the simulation and experimental results. The average error between the numerical and experimental results was 1.37% for C_l, 6.73% for C_d, and 6.84% for L/D. This discrepancy is attributed to factors such as experimental model surface roughness, ambient temperature variation, computational model accuracy, and experimental inaccuracy. Because of the high computational cost associated with higher-order computational models, all numerical analyses were performed using the k-ω SST model, as discussed earlier in Section 2.2.3. Pure air properties (without moisture and salt content) were used for simulation, whereas air may contain impurities during experimentation, which could be another reason for the discrepancy in the results.

3.2 Experimental Repeatability

Experiment repeatability was ensured by plotting the results of three independent trials on the same set of axes for comparison. The repeatability results for the SG6043 baseline airfoil are presented in Fig. 14. No significant difference was noted in the results of the three trials, and the trends were also consistent. During the experimentation, an average error of 0.31%, 1.39%, and 2.1% was obtained for each set of C_l, C_d, and L/D. All experiments were performed under the same atmospheric conditions to ensure that aerodynamic coefficients did not change.

3.3 Aerodynamic Performance of Distinct Leading-Edge Protuberances

3.3.1 Sinusoidal Protuberances

The aerodynamic variables, such as the maximum lift coefficient ($C_{l\ max}$), stall angle (α_{stall}), and maximum lift to drag ratio ($(L/D)_{max}$), for various configurations and airfoils are listed and compared with baseline values in Table 7. For the SG6043 airfoil, the lowest amplitude configurations exhibited a delay in the stall angle of 2°. All the configurations indicated that $C_{l\ max}$ and $(L/D)_{max}$ values were lower those at the baseline. When the amplitude was maintained constant, we noted an increase in $C_{l\ max}$ and $(L/D)_{max}$ with increases in wavelength and constant wavelength. Moreover, $(L/D)_{max}$ decreased with an increase in amplitude, whereas no considerable change was observed in $C_{l\ max}$ with an increase in the amplitude. For the E216 airfoil, a stall delay of 2° was observed for the lowest amplitude configurations.

For A4.5W31.5 & A4.5W64.5 configurations, the stall delay was associated with improved $C_{l\ max}$ and $(L/D)_{max}$. All the other configurations exhibited a degradation of $C_{l\ max}$ and $(L/D)_{max}$ but not the stall angle.

(a) Lift coefficient   (b) Drag coefficient   (c) Lift to drag ratio
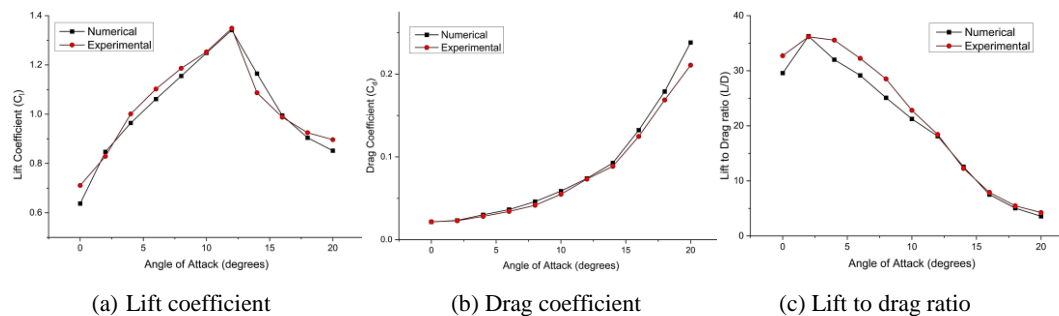
Fig. 13. Validation of numerical results for E216 baseline airfoil.

| (a) Lift coefficient | (b) Drag coefficient | (c) Lift to drag ratio |
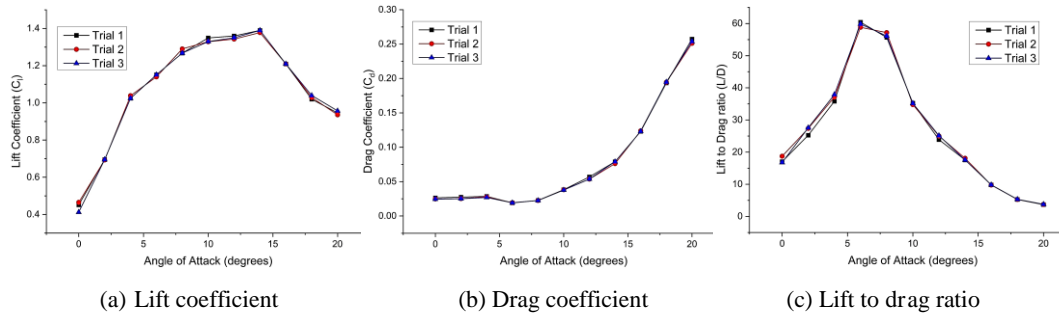
Fig. 14. Experimental repeatability for SG6043 baseline airfoil.
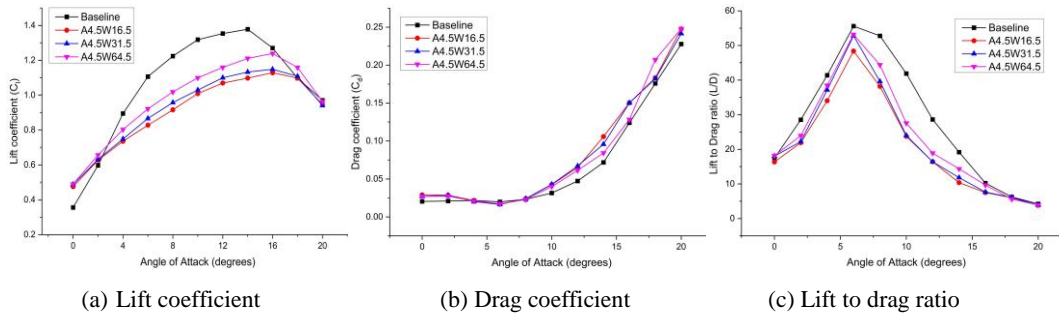
| (a) Lift coefficient | (b) Drag coefficient | (c) Lift to drag ratio |

Fig. 15. Effect of the wavelength of sinusoidal protuberances on the aerodynamic parameters of SG6043 airfoil at constant amplitude.

| (a) Lift coefficient | (b) Drag coefficient | (c) Lift to drag ratio |
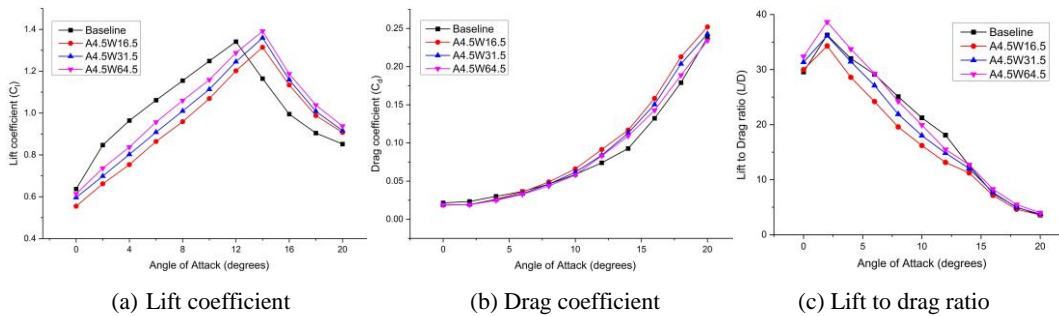
Fig. 16. Effect of the wavelength of sinusoidal protuberances on the aerodynamic parameters of E216 airfoil at constant amplitude.

For configurations having the same amplitude, $C_{l\,max}$ and $(L/D)_{max}$ increased with the wavelength. However, for constant wavelength, $C_{l\,max}$ and $(L/D)_{max}$ decreased with an increase in the amplitude. Hence, low amplitude and high wavelength are recommended to achieve the highest aerodynamic performance. These numerical results are plotted along with the baseline SG6043 and E216 results in Figs. 15 and 16, respectively. For SG6043, we noted a degradation in the prestall lift performance and a marginal improvement in the post-stall lift. The zero-lift coefficient increased for all the protuberance configurations. The drag values were unaffected until an AoA of 8°, after which protuberance configurations resulted in higher drag values than the baseline. All configurations had L/D ratios lower than that at the baseline. For E216, as indicated by lift curves plotted in Fig. 16a, a degradation in prestall lift performance, delay in the stall, and an improvement in $C_{l\,max}$ were noted. In addition, we

Table 7 Comparison of the effect of sinusoidal protuberances on the aerodynamic performance of E216 and SG6043 airfoil

Configuration	E216			SG6043		
	C_{lmax}	α_{stall}	$(L/D)_{max}$	C_{lmax}	α_{stall}	$(L/D)_{max}$
A4.5W16.5	1.31	14	34.3	1.12	16	48.39
A4.5W31.5	1.36	14	36.1	1.14	16	52.83
A4.5W64.5	1.39	14	38.6	1.23	16	53.16
A9W16.5	1.28	12	30.7	1.15	14	45.71
A9W31.5	1.31	12	32.3	1.17	14	48.88
A9W64.5	1.34	12	34.6	1.25	14	51.89
A16.5W16.5	1.21	12	27.3	1.13	14	44.12
A16.5W31.5	1.25	12	29.5	1.18	14	47.32
A16.5W64.5	1.30	12	32.4	1.26	14	48.91
Baseline	1.35	12	36.2	1.37	14	55.6

observed improved poststall lift performance. The drag values were not much affected until an AoA of 10°, and after that, protuberance configurations resulted in higher drag values than the baseline.

Among the configurations tested, A4.5W64.5 showed the highest drag at high AoAs. Although the L/D ratio was below the baseline for most of the AoA, the protuberance configurations yielded higher $(L/D)_{max}$ values. Experimental force measurements were performed only for the A9W64.5 configuration, which yielded optimal results in the numerical analysis. The results were compared with baseline results (Figs. 17 and 18). For the SG6043 airfoil, prestall lift degradation, poststall lift improvement, and increased zero lift coefficient were observed in the experimental lift curve depicted in Fig. 17(a). The drag values shown in Fig. 17 (b) are similar to the baseline in the entire AoA range, which contradicts the numerical results. This could be due to the drag measurement technique that uses strain gauges. More accurate drag measurements can be obtained using the wake survey method, which is beyond the scope of the present study. The L/D ratio curve of A9W64.5 was below the baseline curve for most of the AoA range (Fig. 17(c)). Similarly, for the E216 airfoil, prestall lift degradation was observed in experimental lift curves shown in Fig. 18(a). No stall delay and improvement in the poststall lift were noted, which is similar to numerical simulations. The drag curves shown in Fig. 18(b) indicate the protuberance configuration exhibits a higher drag than baseline in the entire AoA range, which is partially captured in simulations. The L/D ratio curve

of A9W64.5 was below the baseline curve for most of the AoA range presented in Fig. 18(c).

3.3.2 Triangular Protuberances

The numerical results for E216 and SG6043 airfoils with triangular protuberances are listed and compared with baseline values in Table 8. For the SG6043 airfoil, a 2° delay in stall was noted for the lowest amplitude configuration. A degradation in $C_{l\ max}$ and $(L/D)_{max}$ was observed for all the configurations. The model with the lowest amplitude and highest wavelength (i.e., A4.5W64.5) had $C_{l\ max}$ and $(L/D)_{max}$ that were comparable to baseline values.

Table 8 Comparison of the effect of triangular protuberances the on aerodynamic performance of E216 and SG6043 airfoils

Configuration	E216			SG6043		
	C_{lmax}	α_{stall}	$(L/D)_{max}$	C_{lmax}	α_{stall}	$(L/D)_{max}$
A4.5W16.5	1.39	16	38.3	1.19	16	49.57
A4.5W31.5	1.46	16	40.6	1.24	16	52.3
A4.5W64.5	1.52	16	42.3	1.31	16	54.52
A9W16.5	1.29	14	30.1	1.15	14	48.12
A9W31.5	1.31	14	33.9	1.21	14	51.09
A9W64.5	1.36	14	35.4	1.29	14	53.11
A16.5W16.5	1.24	12	29.7	1.13	14	46.22
A16.5W31.5	1.27	12	31.3	1.18	14	48.17
A16.5W64.5	1.32	12	33.8	1.26	14	50.35
Baseline	1.35	12	36.2	1.37	14	55.6
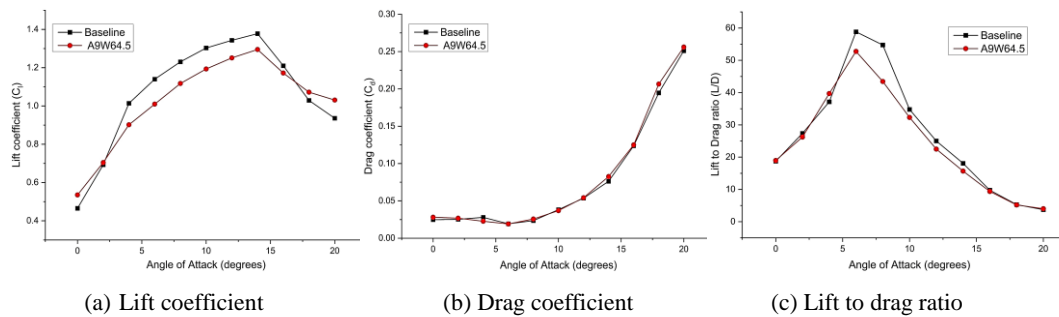
(a) Lift coefficient	(b) Drag coefficient	(c) Lift to drag ratio

Fig. 17. Experimental results of SG6043 baseline and A9W64.5 sinusoidal protuberance model.

(a) Lift coefficient	(b) Drag coefficient	(c) Lift to drag ratio
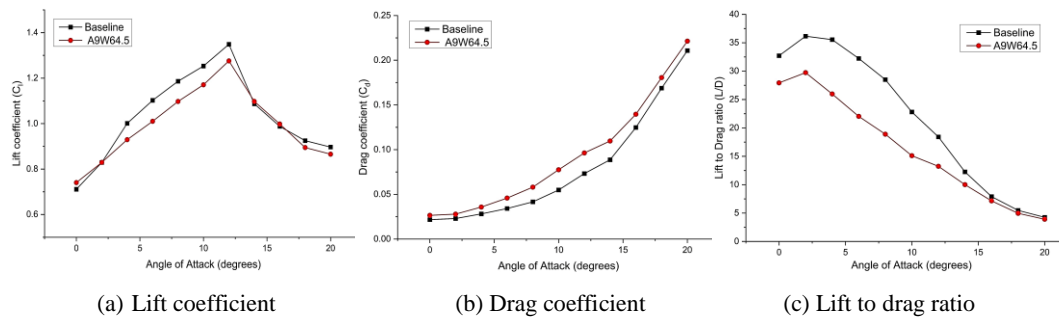
Fig. 18. Experimental results of E216 baseline and A9W64.5 sinusoidal protuberance model.

For the E216 airfoil, a stall delay of 2° to 4° was observed for A4.5 and A9 models. An improvement in $C_{l\,max}$ and $(L/D)_{max}$ was observed for the lowest amplitude configuration. For both the airfoil profiles, when the amplitude was maintained constant, $C_{l\,max}$ and $(L/D)_{max}$ increased with an increase in wavelength, whereas for constant wavelength, $C_{l\,max}$ and $(L/D)_{max}$ decreased with an increase in the amplitude.

The numerical results of C_l, C_d, and L/D of various models of the SG6043 airfoil are plotted along with baseline values shown in Fig. 19. The lift curves in Fig. 19 (a) indicated a degradation in the prestall lift for all the configurations and a slight improvement in the poststall lift for a higher-wavelength model. The protuberance configurations yielded a higher zero C_l. Despite a delay in the stall, it was associated with a reduction in $C_{l\,max}$. The drag curves in Fig. 19 (b) demonstrate that the drag values of protuberance configurations were higher than the baseline at A0A > 12°. The configuration with the lowest amplitude and lowest wavelength (i.e., A4.5W16.5) exhibited the highest drag in the high A0A range. The L/D curves presented in Fig. 19(c) indicated that all the protuberance configurations yielded lower L/D values than the baseline.

Experimental force measurements were performed using the SG6043 airfoil for the A9W64.5 model and compared with baseline experimental values (Fig. 20). A prestall lift degradation followed by a marginal increase in the poststall lift was noted at an AoA of >16°. The zero-lift coefficient was higher for protuberance configuration, which is also observed in numerical simulations. The drag values in the low

AoA range were comparable to baseline. By contrast, at AoA > 16°, the baseline had a higher drag than the protuberance configuration, which contradicts numerical simulation results.

Because drag measurement and prediction in the poststall region are challenging and sensitive to many variables, a dedicated study should be performed to address the drag analysis in the poststall region. The L/D ratio values were higher than baseline for protuberance configurations in the low AoA range, whereas in the high AoA range, they were comparable to baseline values. The numerical results for the E216 baseline airfoil were compared with the modified models (Fig. 21). From the lift curves shown in Fig. 21(a), a degradation in the prestall lift and an improvement in the poststall lift were noted. A delay in the stall was associated with an improvement in $C_{l\,max}$. The drag curves in Fig. 21 (b) indicate that the drag coefficient values of protuberance configurations are comparable to baseline until an AoA of 10° but higher at high AoA.

The L/D curves of protuberance configurations were above the baseline curve (Fig. 21c). An increasing trend with wavelength was noted, and the highest $(L/D)_{max}$ was observed for the A4.5W64.5 configuration. The experimental force measurements were performed for the A9W64.5 configuration at an optimal amplitude and the highest wavelength. These experimental nondimensional coefficients were compared with baseline experimental values (Fig. 22). From the lift curves shown in Fig. 22a, we observed an improvement in lift performance in both prestall and poststall regimes.

| (a) Lift coefficient | (b) Drag coefficient | (c) Lift to drag ratio |
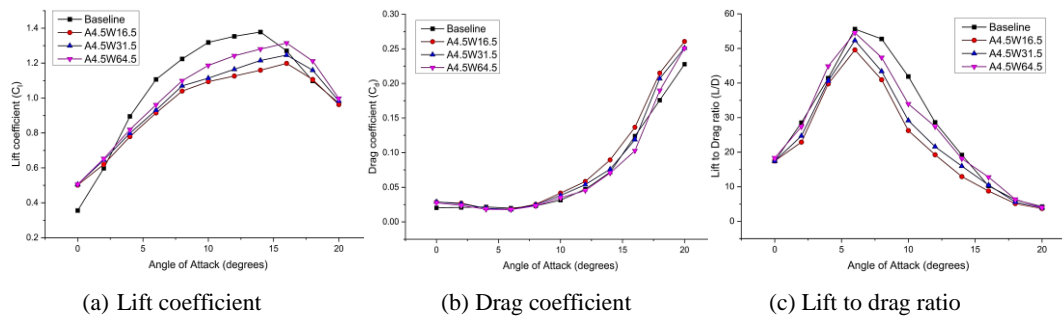
Fig. 19. Effect of the wavelength of triangular protuberances on the aerodynamic parameters of SG6043 airfoil at constant amplitude.

| (a) Lift coefficient | (b) Drag coefficient | (c) Lift to drag ratio |

Fig. 20. Experimental results of SG6043 baseline and A9W64.5 triangular protuberance model.

| (a) Lift coefficient | (b) Drag coefficient | (c) Lift to drag ratio |
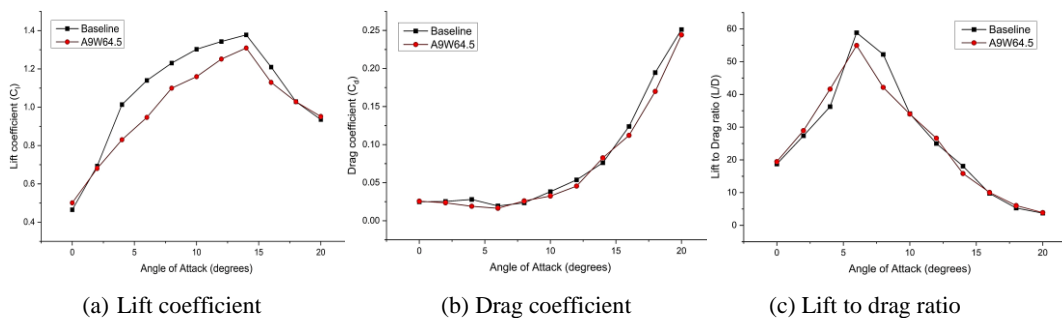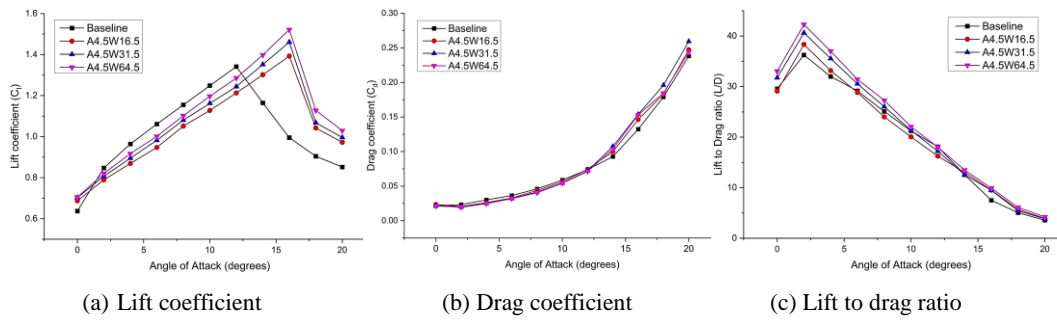
Fig. 21. Effect of wavelength of triangular protuberances on the aerodynamic parameters of E216 airfoil at constant amplitude.

| (a) Lift coefficient | (b) Drag coefficient | (c) Lift to drag ratio |

Fig. 22. Experimental results of E216 baseline and A9W64.5 triangular protuberance model.

| (a) Lift coefficient | (b) Drag coefficient | (c) Lift to drag ratio |
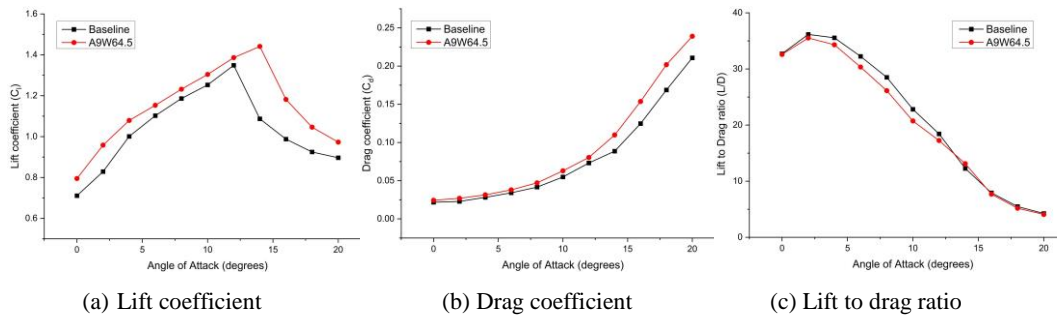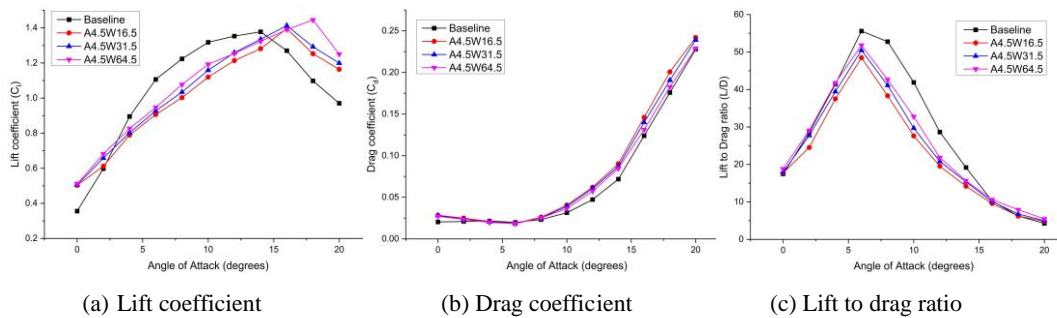
Fig. 23. Effect of the wavelength of slot protuberances on the aerodynamic parameters of SG6043 airfoil at constant amplitude.

Only poststall improvement was captured in numerical simulation. The drag curves shown in Fig. 22(b) indicated that the drag values of protuberance configurations were higher than baseline at a high AoA, which is also observed in simulations. The L/D ratio values were comparable to baseline values (Fig. 22 (c)).

3.3.3 Slot Protuberances

The numerical results of various configurations for E216 and SG6043 airfoils are listed and compared in Table 9. All the configurations of both the airfoils exhibited a delay in the stall in the range of 2° to 4°. For the E216 airfoil, most of the protuberance configurations improved the $C_{l\,max}$ in addition to a delay in stall. The lowest amplitude configurations exhibited an improvement in the L/D$_{max}$. A degradation of prestall lift was noted for all configurations, whereas a slight improvement in poststall lift was noted for high wavelength designs according to lift curves shown in Fig. 23(a).

Table 9 Comparison of the effect of slot protuberances on the aerodynamic performance of E216 and SG6043 airfoils

Configuration	E216			SG6043		
	C_{lmax}	α_{stall}	$(L/D)_{max}$	C_{lmax}	α_{stall}	$(L/D)_{max}$
A4.5W16.5	1.38	16	35.8	1.39	16	48.47
A4.5W31.5	1.42	16	37.1	1.41	16	50.46
A4.5W64.5	1.45	16	39.3	1.44	18	51.81
A9W16.5	1.36	14	33.8	1.29	16	44.61
A9W31.5	1.39	14	35.9	1.33	16	46.8
A9W64.5	1.41	14	37.6	1.36	16	50.73
A16.5W16.5	1.29	14	29.5	1.22	16	43.40
A16.5W31.5	1.34	14	32.5	1.28	16	45.57
A16.5W64.5	1.37	14	35.7	1.32	16	47.88
Baseline	1.35	12	36.2	1.37	14	55.6
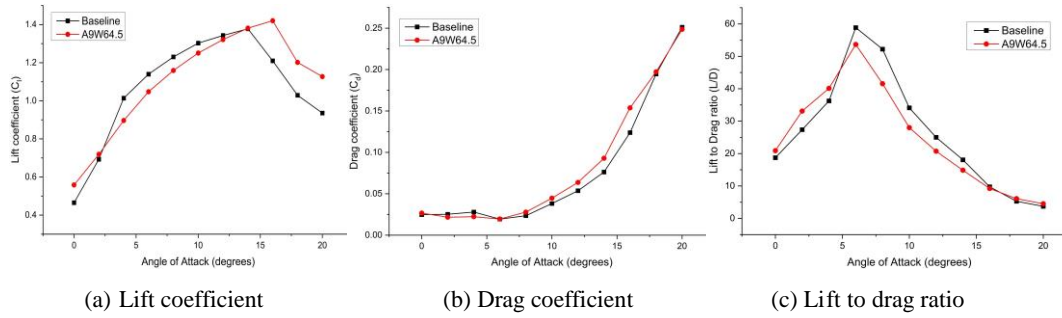
(a) Lift coefficient   (b) Drag coefficient   (c) Lift to drag ratio

Fig. 24. Experimental results of SG6043 baseline and A9W64.5 slot protuberance model.

(a) Lift coefficient   (b) Drag coefficient   (c) Lift to drag ratio
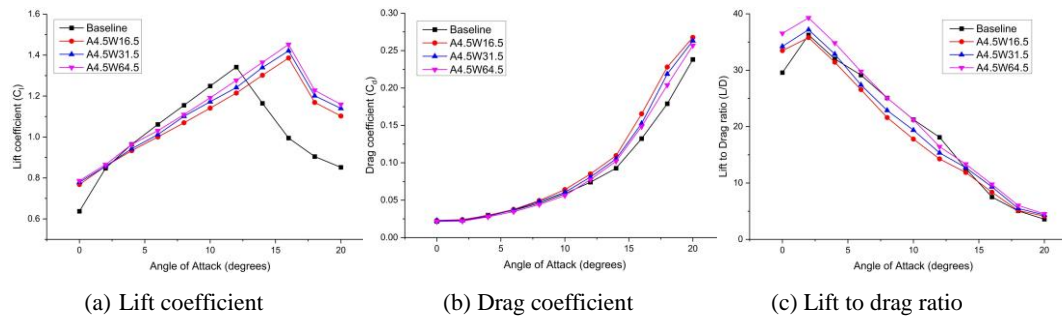
Fig. 25. Effect of the wavelength of slot protuberances on the aerodynamic parameters of E216 airfoil at constant amplitude.

Protuberance designs provide significant zero lift coefficients. Although a stall delay was noted, it is linked to a decrease in $C_{l\ max}$. The drag values of protuberance configurations were significantly higher than baseline values, as shown in Fig. 23(b). The configuration with the smallest amplitude and shortest wavelength, A4.5W16.5, had the most drag in the high AoA range. All the protuberance designs provided lower L/D values than the baseline, as depicted in Fig. 23(c). Experimental force measurements were performed for the A9W64.5 configuration of the maximum wavelength and optimum amplitude. As illustrated in Fig. 24, these experimental nondimensional coefficients were compared with baseline experimental values. A decrease in prestall lift, followed by a significant increase in the stall and poststall areas was noted. As shown in numerical simulations, the zero-lift coefficient was significant for protuberance configurations. The drag values were close to baseline values in the low AoA range; however, the baseline had a lower drag than the protuberance configuration in the stall and post stall regions. Because drag measurement and prediction in the poststall zone are complex and dependent on numerous variables, specific studies should be conducted to address drag analysis in the poststall region. In the low AoA range, the L/D ratio was greater than baseline, but they are equivalent to baseline values in the high AoA range. The numerical results are plotted and compared with the baseline, as depicted in Fig. 25. A significant improvement in poststall lift performance was observed in Fig. 25(a). The prestall lift degradation observed in other protuberance shapes was reduced,

and the lift values were comparable with the baseline configuration. Moreover, an increment in the zero-lift coefficient was noted. The drag curves shown in Fig. 25(b) indicated that slot configurations' drag values were unaffected until an AoA of 12° and for an AoA of >12°; they exhibited higher drag than the baseline. Among the chosen configurations, A4.5W16.5 exhibited the highest drag at a high AoA. An improvement in the L/D_{max} was observed in Fig. 25(c), but in most of the AoA ranges, the L/D values of slot configurations were lower than baseline values. Experimental force experiments were performed using the configuration A9W64.5 slots, the results are presented in Fig. 26. Poststall lift improvement and slight prestall lift degradation were observed in experimental curves shown in Fig. 26(a). The overall drag values for slot configuration were higher than the baseline, and degradation in L/D values were observed until an AoA of 14°.

3.3.4 Airfoils Comparison

For the baseline configuration, SG6043 exhibited a higher α_{stall} and $C_{l\ max}$ than did the E216 airfoil. The maximum lift coefficient of an airfoil is determined by its geometrical parameters: thickness ratio, leading edge radius, camber, and location of the maximum thickness. For the E216 airfoil, the maximum thickness-to-chord ratio $(t/c)_{max}$ was 10.4% at 26.2% chord and the maximum camber was 4.7% at 59% chord. For the SG6043 airfoil, the $(t/c)_{max}$ was 10% at 32.1% chord, and the maximum camber was 5.1% at 53.3% chord. These values contribute to a higher $C_{l\ max}$ exhibited by SG6043. As shown in Table 1, the SG6043 airfoil had a larger leading-edge radius than did the E216 airfoil. A large

(a) Lift coefficient   (b) Drag coefficient   (c) Lift to drag ratio
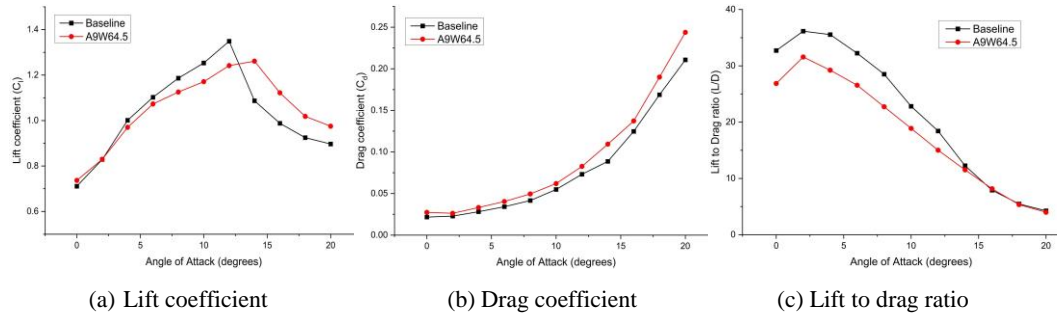
Fig. 26. Experimental results of E216 baseline and A9W64.5 slot protuberance model.

upper surface leading-edge radius alleviated the peak negative pressure coefficients and thus delayed stall to a higher AoA (Roskam and Lan 1997). Hence, the SG6043 airfoil had a larger stall angle than did the E216 airfoil.

The previous sections indicate that the effect of leading-edge protuberances depends on the airfoil to which it is applied. In general, leading-edge protuberances were more beneficial for E216 than SG6043. Among the examined protuberance shapes, the shape of the slot exhibited the highest performance improvement for both the airfoil profiles. Hansen *et al*. (2011) postulated that whenever the maximum thickness position is more aft, the boundary layer expanse was larger, indicating that tubercles might be more advantageous. However, the results of the present study contradict the hypothesis of Hansen. This can be attributed to the chosen profiles, which are similar, and the difference between their positions of the maximum thickness, which was less than 10%.

4. WORKING MECHANISM OF LEADING EDGE PROTUBERANCES

Various studies have provided explanations regarding the working mechanism of leading-edge protuberances (Miklosovic *et al*. 2004; Hansen *et al*. 2011; Fletcher 1975; Van *et al*. 2008; Custodio 2007). The most common mechanisms are the generation of streamwise vortices and an analogy to a vortex generator. In the present study, we analyzed the contours of the vorticity magnitude and turbulent kinetic energy (TKE) in spanwise and streamwise directions to understand the flow physics. Different slices were created in the streamwise direction at the leading edge, mid-chord, trailing edge, and far-field regions. The term "X-vorticity," which is a crucial variable in fluid dynamic, is used to describe the curl of the velocity as a measure of a fluid's rotation in the X-direction (the direction of flow).

4.1 Sinusoidal Protuberances

Figures 27 (a) and (b) presents the contours of X vorticity and overall vorticity magnitude at these slices for A4.5W64.5 configuration with sinusoidal protuberances at an AoA of 0°, respectively. The generation of counter-rotating vortices from the leading-edge protuberance region and its passage in the streamwise direction is evident in Fig. 27 (a).

(a)

(b)
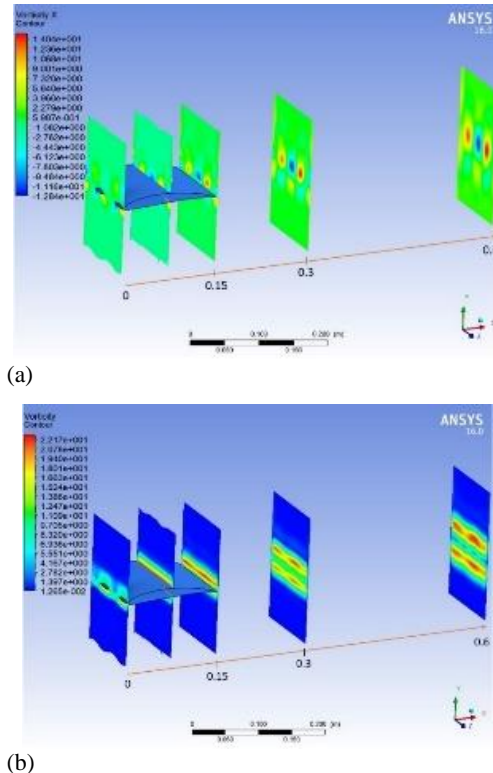
Fig. 27. Contours of (a) X Vorticity and (b) Overall vorticity magnitude at different slices in streamwise direction for A4.5W64.5 configuration with sinusoidal protuberances at an AoA 0°.

After passing through the trailing edge, the downstream flow was split into two high vorticity regions due to the presence of the airfoil, which reveals the extent of wake in Fig. 27 (b). These counter-rotating vortices grew and the intensity decreased in the streamwise direction, as illustrated in Fig. 28. This behavior is similar to streamwise vortices produced by vortex generators (VGs) (Godard and Stanislas 2006). This behavior remained the same even at a stall angle of 16°. In the case of VGs, these vortices energize the boundary layer, thereby delaying flow separation. Further investigation on the flow physics of leading-edge protuberances should be conducted by analyzing TKE contours.

TKE contours at peak and trough regions in the spanwise direction of A4.5W64.5 configuration with

| X = 0.15 m Trailing edge | X = 0.3 m | X = 0.6 m | X = 1 m |
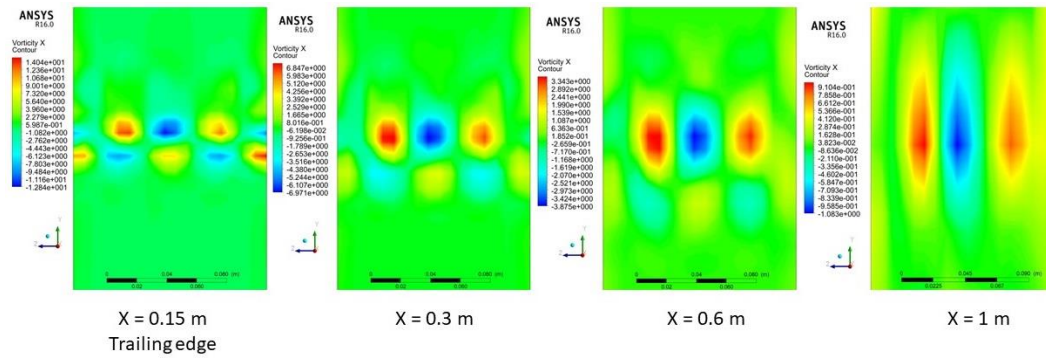
Fig. 28. Counter-rotating vortices generated by sinusoidal protuberances of A4.5W64.5 configuration at an AoA 0° in a streamwise direction.

(a)   (b)
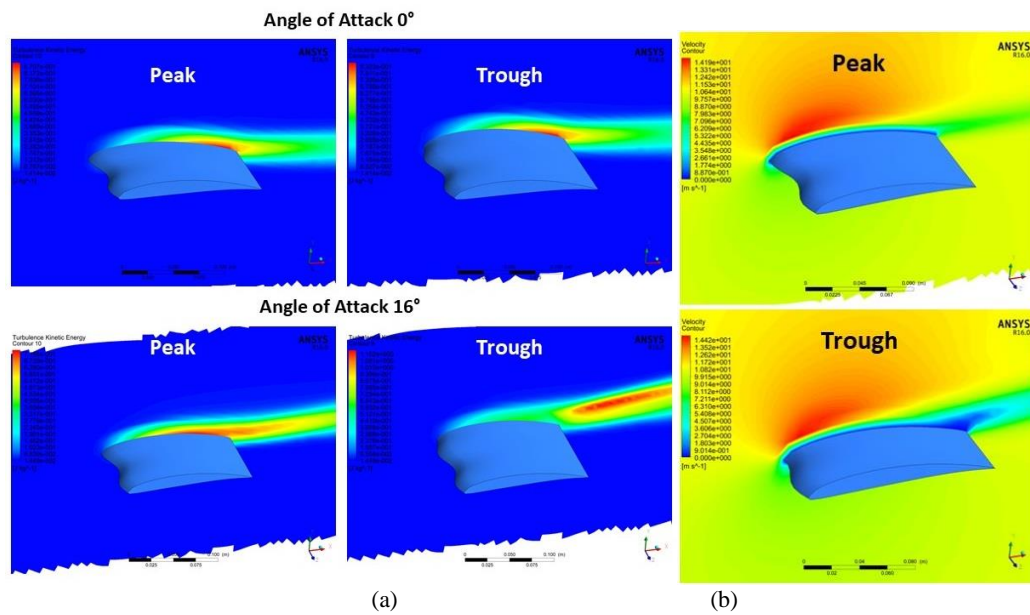
Fig. 29. (a) TKE contours at peak and trough regions at AoAs 0° and 16° (b) Velocity contours at peak and trough regions at 16° angle.

sinusoidal protuberances at zero and stall angles are presented in Fig. 29(a). TKE is a direct measure of turbulence in the flow. At a zero angle, the contours are similar at peak and trough regions. At a stall angle behind the peak region, the flow becomes turbulent at approximately 50% of the chord; then, it reattaches near the trailing edge forming a separation bubble. However, at the trough region, the flow separates near the trailing edge; hence, a significant increase is noted in the TKE magnitude post the trailing edge.

Flow separation occurs first at the trough region. A similar flow behavior was observed in previous wind tunnel experiments (Johari *et al*. 2007) and numerical simulations (Fish and Lauder 2006). This can also be confirmed by analyzing velocity contours at stall angles, as shown in Fig. 29 (b), in which a region of zero velocity can be observed at the trailing edge. The velocity field generated by leading-edge protuberances is variable along the span at a higher AoA, which was observed in previous stereoscopic particle image velocimetry measurements (Esmaeili *et al*. 2018).

4.2 Triangular Protuberances

Triangular protuberances lead to the generation of counter-rotating vortices similar to that of sinusoidal. However, they differ in occurrence, behavior, and strength from other protuberances. They are visualized numerically by considering X vorticity contours at different streamwise slices for the A4.5W64.5 configuration with triangular protuberances at 0° angle (Fig. 30).

From the contours at X = 0.3 m and 0.6 m, we observed that counter-rotating vortex pairs generated behind the adjacent protuberances were symmetric. A marked increase in the size of the vortices after X = 0.6 m in the streamwise direction was associated with a decrease in the intensity. This behavior was similar even at stall angles. The overall vorticity magnitudes were found to be less than that of sinusoidal protuberances.

TKE and velocity magnitude contours at mid-span, peak, and trough regions of the A4.5W64.5 configuration with triangular protuberances at 0° and 18° are shown in Fig. 31. At 0°, no variation in TKE
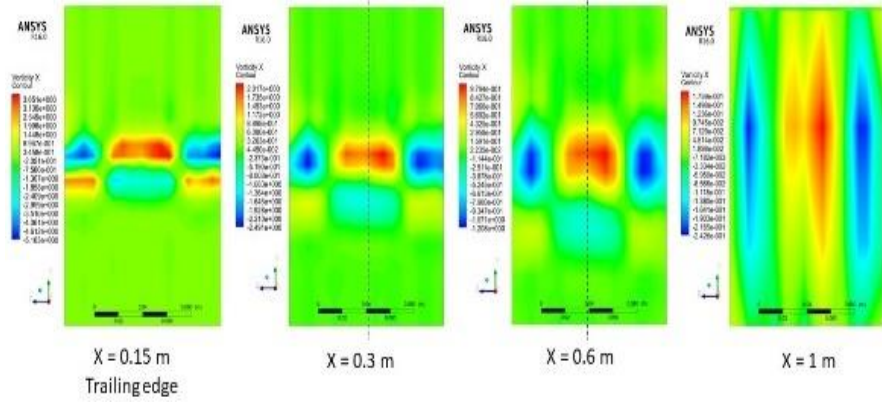
Fig. 30. Counter-rotating vortices are visualized at different streamwise slices for A4.5W64.5 configuration with triangular protuberances at 0° AoA.
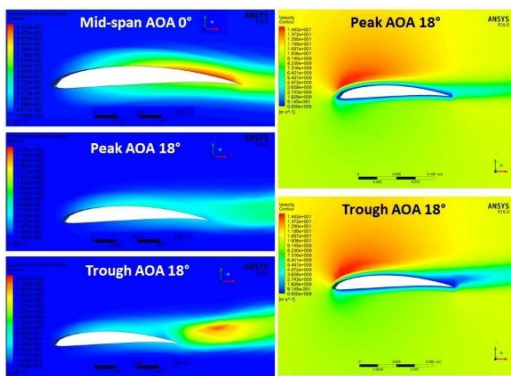
Fig. 31. Contours of TKE and velocity magnitude at peak and trough regions of A4.5W64.5 configuration with triangular protuberances at angles 0° and 18°.

along the spanwise direction was noted. This indicates the formation of a separation bubble close to the trailing edge. At a stall angle (18°), TKE was different at peak and trough regions. No formation of a separation bubble was observed, but the separation started at the trough region. This can be confirmed by examining the velocity magnitude contours at peak and trough regions.

4.3 Slot Protuberances

The leading-edge slots model (i.e., the A4.5W64.5 configuration) generated a pair of counter-rotating vortices associated with two slots, as shown in Fig. 32 (a). These vortices grew in size as they progressed in a streamwise direction, with a decreased intensity. The strength of these vortices was higher than that of triangular and sinusoidal protuberances. Similar vortex formation was observed at stall angles. The TKE field was constant in the spanwise direction. The contours of TKE at 0° and 16° observed at the region of the slot are presented in Fig. 32 (b). In both cases, a turbulent reattachment can be observed near the trailing edge.

The vortex behavior of the three protuberance shapes leads to the following conclusions. All protuberance shapes generate counter-rotating vortices. These vortices develop in size with a decreased intensity in the streamwise direction, similar to the behavior of vortices formed by VGs. Vortex strength is remarkable in slots and the lowest in triangular protuberances. Adjacent triangular protuberances produce symmetric vortices at an imaginary midline between the protuberances.

(a)

(b)
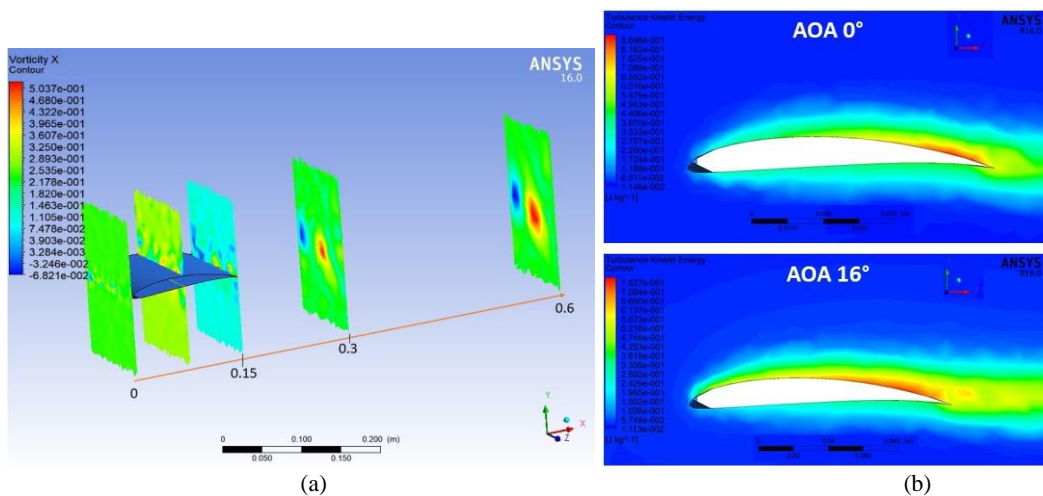
Fig. 32. (a) X vorticity contours at streamwise slices at 0° angle and (b) TKE contours at 0° and 16° taken at slot regions of A4.5W64.5 configuration with slot protuberances.
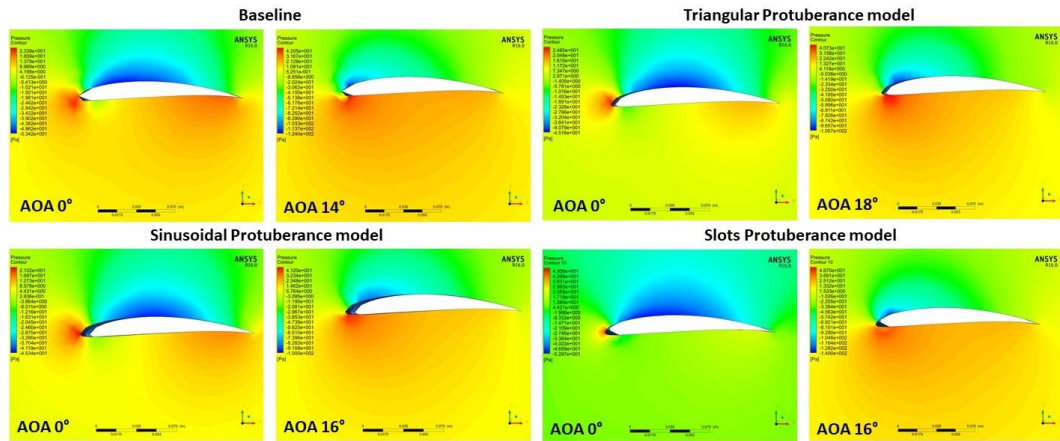
Fig. 33. Comparison of pressure distributions of baseline and modified configurations at 0° and stall angles.
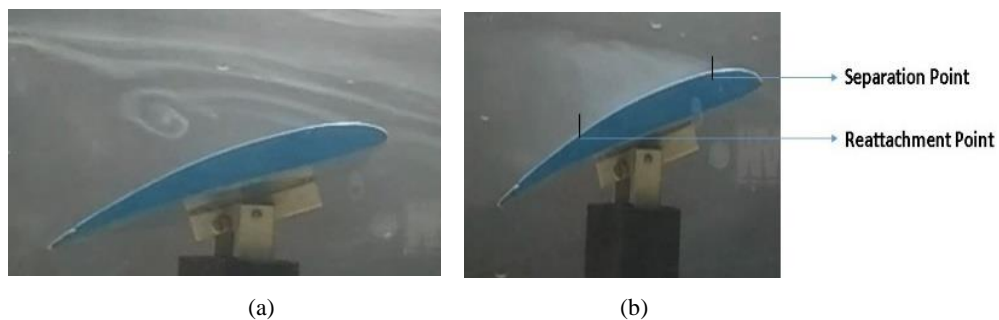
(a)   (b)
Fig. 34. Experimental flow patterns observed using the smoke flow visualization for the SG6043 baseline.

Two unique slots produce a pair of counter-rotating vortices, whereas triangular and sinusoidal produce one pair per protuberance (one at peak and one at trough).

On the basis of the strength of vortices, slots shape result in the best performance in terms of stall delay and improvement in $C_{l\,max}$, which can be explained by vortex lift theory (Polhamus 1968). The behavior is similar to vortices generated by VGs.

However, according to van Van Nierop *et al.* (2008), they can act as VGs because the amplitude and wavelength are larger than the boundary layer thickness. Hence, further numerical investigations should be performed to examine the effect of these protuberances on pressure distribution. The pressure distributions of baseline and modified configurations were compared at 0° and stall angles, as shown in Fig. 33. The leading-edge protuberances modified the pressure distribution significantly.

The static pressure difference between suction and pressure surfaces was small for sinusoidal and triangular protuberances compared with the baseline, whereas slots had significantly higher-pressure differences compared with the baseline. The pressure distribution generated by the airfoil can be studied by analyzing variations in the coefficient of pressure (C_p), a nondimensional parameter in the chordwise direction. Because the difference in static pressure at the upper and lower surfaces of an airfoil manifests in the form of aerodynamic forces, chordwise

variation was considered. These chordwise variations for A9W64.5 configurations for different protuberance shapes were compared with the baseline airfoil (Table 10).

The C_p plots of baseline and slots are almost similar at zero and stall angles. Because the area covered by the C_p plot represents aerodynamic forces generated, both yield the same amount of lift. Among the three protuberance shapes, the sinusoidal shape had the minimum area covered by C_p plots, which are reflected in lift curves. According to both vortex strength and pressure distribution, slots yielded the best performance in terms of $C_{l\,max}$, stall delay, and poststall performance. The relative contribution of the two mechanisms should be examined to determine the exact mechanism responsible for the protuberance effect. The triangular protuberances resulted in higher $C_{l\,max}$ values than the sinusoidal despite having low strength vortices because of the higher static pressure compared with the sinusoidal protuberance. Hence, the mechanism responsible for this result is the change in pressure distribution, not the vortex strength.

5. SMOKE FLOW VISUALIZATION

The behavior of leading-edge protuberances was examined at low speeds by using a smoke flow visualization technique for baseline and modified SG6043 airfoils. The observed flow patterns are presented in Figs. 34–37. The flow pattern and the vortices generated by the straight leading edge, as

Table 10 Comparison of chordwise variation of pressure coefficient for different configurations at zero and stall angles of attack

Configuration	Chordwise Variation of Coefficient of Pressure (C_P)	
	AoA 0°	Stall AoA
Baseline		
A9W64.5 Sinusoidal		
A9W64.5 Triangular		
A9W64.5 Slots		

shown in Fig. 34 (a), were used as reference. A separation bubble formation was observed for the baseline at 15°, as shown in Fig. 34 (b). The separation point was close to the leading edge, and the flow reattached after the mid-chord position.

According to previous studies (Miklosovic *et al.* 2004; Hansen *et al.* 2011; Fletcher *et al.* 1975; van Nierop *et al.* 2008; Custodio 2007), generation of streamwise vortices, which energizes the boundary layer, is responsible for the tubercle effect.

In the present study, because only a single smoke stream was introduced into the flow, we could examine only streamwise flow patterns. A characteristic flow feature was observed at higher angles for sinusoidal and triangular models. A secondary flow emanated from trough regions, as shown in Fig. 35(a). With a further increase in AoA, the secondary flow merged with the primary flow, as shown in Fig. 35 (b). This phenomenon energized the flow at higher angles, resulting in higher poststall lift values observed in experiments. Although the sinusoidal and triangular profiles resulted in similar flow behavior, a difference in secondary flow
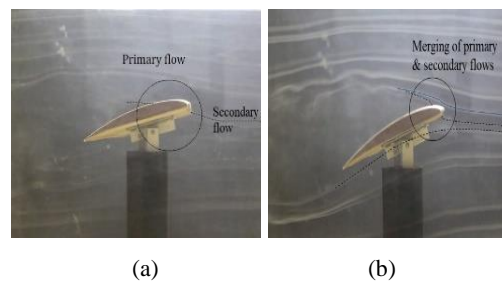
Fig. 35. (a) Secondary flow emerging from the trough region at 10° and (b) Merging of primary and secondary flows at 15° for SG6043 A9W64.5 Triangular model.

volume and strength was noted. The sharp triangular edges guide the flow more effectively to the trough regions, resulting in a high volume of secondary flow. In addition, this reduced the skin friction drag due to the reduction of flow attached to the pressure side of the airfoil. Hence, triangular protuberances are more suitable for the SG6043 airfoil for drag reduction due to off-design penalties at an Re of 10^5 and poststall lift improvement. Further flow

investigation is warranted to determine the behavior of streamwise vortices to understand the stall delay phenomenon. The flow patterns obtained for the slotted model at an AoA of 0° are shown in Fig. 36.

<div align="center">(a)   (b)</div>
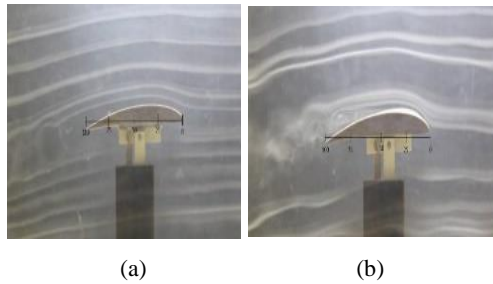
Fig. 36. Streamline patterns of SG6043 A9W64.5 Slotted model with AoA 0° (a) At non-slot region and (b) At slot region.

A difference in the flow behavior was noted at slotted and straight leading-edge regions. At the straight leading-edge region, the streamline followed the airfoil contour shape until 60% of the chord, as shown in Fig. 36 (a). The flow separated at precisely 50% of the chord at the slotted region, resulting in vortices, as shown in Fig. 36 (b). These vortices continued for some distance after passing through the trailing edge. A slight increase in the lift value at zero angle was observed for the slotted model compared with baseline. This result is attributed to additional streamwise vortices generated by leading-edge slots, which contribute to overall vorticity associated with the flow. The additional lift can be explained using vortex flow theory. The flow patterns obtained for the slotted model at higher angles are presented in Fig. 37. Flow phenomena, such as leading edge separation, formation of recirculation regions at the leading edge, and wake regions, were observed at an angle of 15°.

<div align="center">(a)   (b)</div>
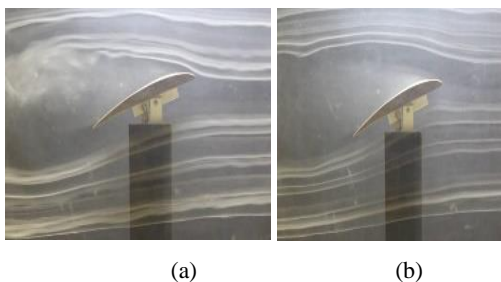
Fig. 37. (a) Leading edge separation and (b) Formation of recirculation region behind the leading edge observed at AoA 15°.

6. CONCLUSIONS

The current study investigated the effect of different leading-edge protuberances, such as sinusoidal, triangular, and slots, on aerodynamic characteristics, such as the C_l, C_d, and L/D ratio of SG6043 and E216 airfoils at an Re of 10^5 experimentally and numerically. The amplitude and wavelength were determined based on the morphological characteristics of the flipper of the humpback whale.

In the case of sinusoidal protuberances, only the smallest amplitude resulted in a 2° stall angle delay for both E216 and SG6043 airfoils. The $C_{l\,max}$ and $(L/D)_{max}$ were improved by 2.88% and 6.22%, respectively, for the E216 airfoil A4.5W64.5 model compared with the baseline model at stall angle. $C_{l\,max}$ and $(L/D)_{max}$ increased with the wavelength for E216 and SG6043 airfoils at a constant amplitude. C_{lmax} and $(L/D)_{max}$ decreased with an increasing amplitude for E216 configurations at a constant wavelength.

For triangular protuberance models, the stall delay for the E216 airfoil ranged from 2° to 4° for A4.5 and A9 models. $C_{l\,max}$ and $(L/D)_{max}$ were improved for the lowest amplitude configurations. $C_{l\,max}$ and $(L/D)_{max}$ increased with the wavelength for both airfoil profiles at a constant amplitude, whereas $C_{l\,max}$ and $(L/D)_{max}$ decreased with the increasing amplitude for both airfoil profiles at a constant wavelength. $C_{l\,max}$ and $(L/D)_{max}$ improved by 11.2% and 14.43%, respectively, for the E216 airfoil when the A4.5W64.5 model was compared with the baseline model at a stall angle.

For slot protuberance models, a comparison of all the configurations of both the airfoils exhibited a stall delay in the range of 2° to 4°. For E216, most configurations improved $C_{l\,max}$ as well as stall delay. This was accompanied by an improvement in $(L/D)_{max}$ for the lowest amplitude configurations. Only low amplitude configurations improved $C_{l\,max}$ for SG6043, but a degradation in $(L/D)_{max}$ was noted.

Slot and triangular protuberances of A4.5 were found to be the most effective in the stall and post-stall regions, respectively. A delay in the onset of stall, an increase in stall C_l, and smooth post-stall lift characteristics are some of the benefits of these protuberances. Low amplitude and high wavelength are recommended to obtain the best aerodynamic performance.

The static pressure difference between suction and pressure surfaces is almost the same for sinusoidal, triangular, and baseline models, whereas slots have a slightly higher pressure difference. The size of the C_P plot was the smallest for sinusoidal configuration, which resulted in the degradation of C_l for this configuration. Slots provide the best performance in terms of $C_{l\,max}$, stall delay, and poststall performance, possibly due to vortex strength and pressure distribution. The shape of the protuberance affects the generation and behavior of counter-rotating vortices, which, in turn, affects its aerodynamic performance. The operating mechanism is a shift in pressure distribution caused by leading-edge modifications instead of the vortices' behavior.

From smoke visualization, a distinct flow feature was observed at higher angles for sinusoidal and triangular models. The trough regions produce secondary flow, which merges with the primary flow. It energizes the flow at higher angles, yielding higher poststall lift values in the experiments.

Although the sinusoidal and triangular profiles produced similar flow behavior, the secondary flow volume and strength differed. The sharp triangular edges effectively guide the flow to the trough regions, resulting in a large volume of secondary flow. Furthermore, these edges reduce skin friction drag by reducing the flow attached to the pressure side of the airfoil. Additional flow investigations are warranted to determine the behavior of streamwise vortices in order to understand the stall delay phenomenon.

ACKNOWLEDGMENTS

REFERENCES

Bolzon, M. D., R. M. Kelso and M. Arjomandi (2017). Force measurements and wake surveys of a swept tubercled wing. *Journal of Aerospace Engineering* 30(3), 04016085.

Cai, C., Z. Zuo, S. Liu and Y. Wu (2015). Numerical investigations of hydrodynamic performance of hydrofoils with leading-edge protuberances. *Advances in Mechanical Engineering* 7(7), 1687814015592088.

Carreira Pedro, H. and M. Kobayashi (2008). Numerical study of stall delay on humpback whale flippers. In *46th AIAA aerospace sciences meeting and exhibit*. p. 584.

Chaudhary, M. K. C. M. and S. Prakash (2021). Experimental Investigations of Small horizontal axis wind turbine rotors. *Journal of Engineering Research* 10(3B).

Chen, T. Y. and L. R. Liou (2011). Blockage corrections in wind tunnel tests of small horizontal-axis wind turbines. *Experimental Thermal and Fluid Science* 35(3), 565-569.

Corsini, A., G. Delibra and A. G. Sheard (2013). On the role of leading-edge bumps in the control of stall onset in axial fan blades. *Journal of Fluids Engineering* 135(8).

Custodio, D. (2007). The effect of humpback whale-like leading edge protuberances on hydrofoil performance. *Worcester Polytechnic Institute*, 75.

Custodio, D., C. W. Henoch and H. Johari (2015). Aerodynamic characteristics of finite span wings with leading-edge protuberances. *AIAA Journal* 53(7), 1878-1893.

Drela, M. and H. Youngren (2001). *XFOIL 6.94 user guide*.

Eleni, D. C., T. I. Athanasios and M. P. Dionissios (2012). Evaluation of the turbulence models for the simulation of the flow over a National Advisory Committee for Aeronautics (NACA) 0012 airfoil. *Journal of Mechanical Engineering Research* 4(3), 100-111.

Esmaeili, A., H. E. C. Delgado and J. M. M. Sousa (2018). Numerical simulations of low-Reynolds-number flow past finite wings with leading-edge protuberances. *Journal of Aircraft* 55(1), 226-238.

Fernandes, I., Y. Sapkota, T. Mammen, A. Rasheed, C. Rebello and Y. H. Kim (2013). Theoretical and experimental investigation of leading edge tubercles on the wing performance. In *2013 Aviation Technology, Integration, and Operations Conference* (p. 4300).

Fish, F. E. (2020). Biomimetics and the application of the leading-edge tubercles of the humpback whale flipper. In *Flow control through bio-inspired leading-edge tubercles* (pp. 1-39). Springer, Cham.

Fish, F. and G. V. Lauder (2006). Passive and active flow control by swimming fishes and mammals. *Annual Review of Fluid Mechanics* 38, 193-224.

Fletcher, N. H. (1975). Mechanics of flight. *Physics Education* 10(5), 385.

FLUENT (2014). 15.0. Theory Guide.

Gawad, A. F. A. (2013). Utilization of whale-inspired tubercles as a control technique to improve airfoil performance. *Transaction on Control and Mechanical Systems* 2(5), 212-218.

Godard, G. and M. Stanislas (2006). Control of a decelerating boundary layer. Part 1: Optimization of passive vortex generators. *Aerospace Science and Technology* 10(3), 181-191.

Guerreiro, J. L. E. and J. M. M. Sousa (2012). Low-Reynolds-number effects in passive stall control using sinusoidal leading edges. *AIAA Journal* 50(2), 461-469.

Gupta, R. K., V. Warudkar, R. Purohit and S. S. Rajpurohit (2017). Modeling and aerodynamic analysis of small scale, mixed airfoil horizontal axis wind turbine blade. *Materials Today: Proceedings* 4(4), 5370-5384.

Hansen, K. L., R. M. Kelso and B. B. Dally (2011). Performance variations of leading-edge tubercles for distinct airfoil profiles. *AIAA Journal* 49(1), 185-194.

Jin, W. and Y. G. Lee (2015). Drag reduction design for a long-endurance electric powered UAV. *International Journal of Aeronautical and Space Sciences* 16(2), 311-324.

Johari, H., C. Henoch, D. Custodio and A. Levshin (2007). Effects of leading-edge protuberances on airfoil performance. *AIAA Journal* 45(11), 2634-2642.

Joseph, J., A. Sathyabhama and S. Sridhar (2022). Experimental and numerical analysis of humpback whale inspired tubercles on swept

wings. *Aircraft Engineering and Aerospace Technology*.

Kline, S. J. (1953). Describing uncertainty in single sample experiments. *Mechanical Engineering* 75, 3-8.

Menter, F. R., M. Kuntz and R. Langtry (2003). Ten years of industrial experience with the SST turbulence model. *Turbulence, Heat and Mass Transfer* 4(1), 625-632.

Miklosovic, D. S., M. M. Murray and L. E. Howle (2007). Experimental evaluation of sinusoidal leading edges. *Journal of Aircraft* 44(4), 1404-1408.

Miklosovic, D. S., M. M. Murray, L. E. Howle and F. E. Fish (2004). Leading-edge tubercles delay stall on humpback whale (Megaptera novaeangliae) flippers. *Physics of Fluids* 16(5), L39-L42.

New, T. H., Z. Y. Wei and Y. D. Cui (2015). On the effectiveness of leading-edge modifications upon cambered SD7032 wings. In *Conference proceedings of 10th Pacific symposium on flow visualization and image processing*, Naples, Italy.

Patankar, S. V. (2018). *Numerical heat transfer and fluid flow*. CRC press.

Polhamus, E. C. (1968). *Application of the leading-edge-suction analogy of vortex lift to the drag due to lift of sharp-edge delta wings*. National Aeronautics and Space Administration.

Roskam, J. and C. T. E. Lan (1997). *Airplane aerodynamics and performance*. DAR corporation.

Rostamzadeh Torghabeh, N., R. Kelso, B. Dally and K. Hansen (2013). The effect of undulating leading-edge modifications on NACA 0021 airfoil characteristics. *Physics of Fluids* 25(11), 1-19

Schreck, S. J., N. N. Sørensen and M. C. Robinson (2007). Aerodynamic structures and processes in rotationally augmented flow fields. *Wind Energy: An International Journal for Progress and Applications in Wind Power Conversion Technology* 10(2), 159-178.

Siram, O., N. Sahoo and U. K. Saha (2022). Wind tunnel tests of a model small-scale horizontal-axis wind turbine developed from blade element momentum theory. *Journal of Energy Resources Technology* 144(6).

Skillen, A., A. Revell, J. Favier, A. Pinelli and U. Piomelli (2013). Investigation of wing stall delay effect due to an undulating leading edge: An LES study. In *Eighth International Symposium on Turbulence and Shear Flow Phenomena*. Begel House Inc.

Sreejith, B. K. and A. Sathyabhama (2020). Experimental and numerical study of laminar separation bubble formation on low Reynolds number airfoil with leading-edge tubercles. *Journal of the Brazilian Society of Mechanical Sciences and Engineering* 42(4), 1-15.

Stanway, M. J. (2008). *Hydrodynamic effects of leading-edge tubercles on control surfaces and in flapping foil propulsion* (Doctoral dissertation, Massachusetts Institute of Technology).

Van Nierop, E. A., S. Alben and M. P. Brenner (2008). How bumps on whale flippers delay stall: an aerodynamic model. *Physical Review Letters* 100(5), 054502.

Versteeg, H. K. and W. Malalasekera (2007). *An introduction to computational fluid dynamics: the finite volume method*. Pearson education.

Weber, P. W., L. E. Howle and M. M. Murray (2010). Lift, drag, and cavitation onset on rudders with leading-edge tubercles. *Marine Technology and SNAME News* 47(01), 27-36.

Wei, Z., T. H. New and Y. D. Cui (2018). Aerodynamic performance and surface flow structures of leading-edge tubercled tapered swept-back wings. *AIAA Journal* 56(1), 423-431.

Zhang, M. M., G. F. Wang and J. Z. Xu (2013). Aerodynamic control of low-Reynolds-number airfoil with leading-edge protuberances. *AIAA Journal* 51(8), 1960-1971.

Zhang, M. M., G. F. Wang and J. Z. Xu (2014). Experimental study of flow separation control on a low-Re airfoil using leading-edge protuberance method. *Experiments in Fluids* 55(4), 1-13.